Resonant magnetic and multipolar scattering at the neodymium $L_{2,3}$ absorption edges in the antiferroquadrupolar phase of NdMg

Oana Bunău,* Rose Marie Galéra, Yves Joly, Mehdi Amara, and Sorana Emilia Luca
Institut Néel, CNRS–UJF, BP 166, 38042 Grenoble Cedex 9, France

Carsten Detlefs
European Synchrotron Radiation Facility, BP 220, 38043 Grenoble Cedex 9, France
(Received 24 September 2009; revised manuscript received 11 February 2010; published 2 April 2010)

The CsCl-type antiferromagnetic compound NdMg presents below T_N=61 K a second spontaneous transition at 35 K, associated with an antiferroquadrupolar (AFQ) ordering of the $\langle P_{xy}\rangle$ quadrupolar component. The AFQ ordering induces a new charge periodicity that is detected by the onset of satellite reflections in the x-ray Bragg diffraction pattern. This multipolar scattering is observed in normal Thomson scattering conditions. In the present work, we report a study of both multipolar and magnetic resonant x-ray scattering in NdMg. For both the quadrupolar and magnetic satellites, a clear resonant enhancement is observed at the Nd $L_{2,3}$ absorption edges. The quadrupolar origin of the $(\frac{h}{2}0\frac{l}{2})$-type reflections is unambiguously confirmed by the thermal and azimuthal dependence of their intensity. At the resonance, the magnetic satellites reveal a complex multipeak shape. Two methods, the finite-difference method (FDM) and the multiple scattering method within the muffin-tin approximation (MST-MT), have been used to simulate the experimental spectra. It turns out that the resonance of the quadrupolar satellites can be well accounted for within the FDM approach. For the magnetic resonance, the MST-MT approach including the spin-orbit coupling is best suited. The positions in energy of the dipolar electric E1 transitions to the final 5*d* conduction states are well predicted.

DOI: 10.1103/PhysRevB.81.144402 PACS number(s): 71.20.Eh, 75.25.−j, 78.20.Bh, 78.70.Ck

I. INTRODUCTION

The 4*f* electronic distribution of rare earths (REs) possesses the ability to distort in presence of anisotropic electrostatic fields when $L_{4f}\neq 0$. Within a crystal, this anisotropy expresses itself through the crystalline electric field interactions. The resulting asphericity of the 4*f* electronic distribution is described in terms of 4*f* electric quadrupoles. In condensed RE systems, interactions can exist between these quadrupoles. The mechanism of these quadrupolar interactions varies according to the insulating or metallic nature of the system. It ranges from the purely lattice-mediated interactions in oxides exhibiting a cooperative Jahn-Teller effect to indirect Ruderman-Kittel-Kasuya-Yoshida (RKKY)-type interactions in metallic compounds.[1–3]

In a few 4*f* systems, oxides or metals with reduced spin interactions, quadrupolar interactions can drive within the paramagnetic state a purely orbital ordering. For instance, purely orbital orderings have been reported in the series of the orthovanadates ($DyVO_4$, $TbVO_4$, and $TmVO_4$), and in cubic or tetragonal metallic compounds such as TmZn, TmCd, CeB_6, or DyB_2C_2.[1,3–6]

Even though the vast majority of metallic RE systems order magnetically at low temperature, the 4*f* orbital degrees of freedom have a crucial influence on the ordered state properties. They may determine the type (first order or second order) of the magnetic phase transitions, the nature of the ordered phases, and all the related properties. Because of the spin-orbit coupling of the 4*f* electrons, the indirect RKKY-type exchange coupling drives concomitantly the ordering of the spins and the quadrupoles. Thus the quadrupolar moment should be considered as a secondary order parameter. In cubic systems, the stabilization of complex multiaxial magnetic arrangements is ascribed to "negative" quadrupolar interactions (antiferroquadrupolar couplings). This is well illustrated in many CsCl-type RE intermetallics such as NdMg.[3] In the antiferromagnetic phase (T_N=61 K), NdMg displays a spontaneous transition at T_R=35 K between the collinear magnetic structure that settles at T_N and a double-***k*** structure.[7] The collinear magnetic structure is associated with a ferroquadrupolar arrangement of the $\langle O_2^0\rangle$ quadrupolar component (phase I in Fig. 1) while the double-***k*** structure is associated with an antiferroquadrupolar (AFQ) arrangement of the $\langle P_{xy}\rangle$ component (phase II in Fig. 1). This type of antiferroquadrupolar arrangement is indirectly but unambiguously identified by neutron-diffraction studies on single crystals and under magnetic fields. It is of crucial interest for the evaluation of x-ray techniques applied to the investigation of quadrupolar orderings. Therefore, NdMg can be a model system for validating the multipolar Thomson

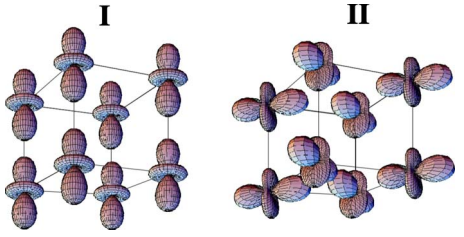

FIG. 1. (Color online) Sketches of the quadrupolar arrangement in NdMg. In phase I, between T_N=61 K and T_R=35 K, the single-***k*** collinear antiferromagnetic structure is associated with a ferroquadrupolar arrangement of the $\langle O_2^0\rangle$ quadrupolar component. Below T_R in phase II, the double-***k*** structure with the magnetic moments along the twofold axes is associated with the antiferroquadrupolar arrangement of the $\langle P_{xy}\rangle$ components.

scattering as a probe for antiferroquadrupolar arrangements.[8] Indeed x-ray satellites reflections, associated with the new charge periodicity resulting from the antiferroquadrupolar wave, were clearly observed below T_R. Although based on an easily interpreted and formalized phenomenon, the multipolar Thomson scattering technique suffers from the weakness of the scattering amplitudes. In front of such difficulties and by analogy with magnetic x-ray scattering, one may consider taking advantage of resonant x-ray scattering (RXS) in order to amplify the quadrupolar scattering.

The first orbital RXS studies were focused on the investigation of $3d$ orbital ordering in perovskite-type manganites or vanadates.[9–12] Results on $3d$ compounds prompted studies on f-electron systems and the observation of RXS satellites ascribed to an antiferroquadrupolar ordering in DyB_2C_2 were soon reported.[13–15] A number of RXS studies devoted to the exploration of multipolar orderings followed in $5f$-based systems at the $M_{4,5}$ absorption edges of actinides.[16–21] Except for the investigation of the intriguing $(Ce,La)B_6$ compounds, very few studies have been performed at the $L_{2,3}$ edges of the rare earths.[22,23] In all of these investigations, the RXS technique has been applied to controversial systems supposed, from other indirect techniques, to show a multipolar ordering. RXS studies on a well-characterized multipolar system would allow not only qualification of this technique but also comparison with nonresonant multipolar scattering. NdMg is ideally suited for such a study with the additional practical advantage of an uncommon resistance to oxidization.

In this paper, we report an experimental study of the multipolar and magnetic resonant scattering at the $L_{2,3}$ edges of neodymium in a single crystal of NdMg. With the aim to improve the understanding of the resonant processes, the experimental spectra are compared to *ab initio* calculated spectra. The simulations are performed in a monoelectronic approach using the FDMNES code[24–26] (standing for finite-difference method near-edge structure). Two different methods, the finite-difference method (FDM) and the multiple scattering theory within the muffin-tin approximation (MST-MT) are used. The experimental conditions are presented in Sec. II. Section III deals with the *ab initio* calculations of the spectra. The experimental results are compared with the simulations in Sec. IV. The last section summarizes and concludes the paper.

II. EXPERIMENTAL

A. Sample

The NdMg compound crystallizes in the cubic CsCl-type structure (space group $Pm\bar{3}m$) with a cell parameter $a=3.8$ Å at room temperature. It orders antiferromagnetically at $T_N=61$ K within a single-$\boldsymbol{k}$ collinear magnetic structure: $\vec{k}=[\frac{1}{2}00]$ propagates the magnetic moment along [100]. In this phase (phase I), only the $\langle O_2^0\rangle$ quadrupolar component orders within a ferroquadrupolar arrangement as illustrated in Fig. 1. Through the magnetoelastic coupling, it results a tetragonal symmetry lowering with $(a-c)/a<1$.[27] At $T_R=35$ K, a second spontaneous magnetic transition is observed that corresponds to the change into a double-$\boldsymbol{k}$ structure with moments along twofold axes (phase II). It is described by the respective Fourier components and wave vectors: $\vec{m}_1=[\frac{1}{\sqrt{2}}00]$, $\vec{k}_1=[\frac{1}{2}00]$ and $\vec{m}_2=[0\frac{1}{\sqrt{2}}0]$, $\vec{k}_2=[0\frac{1}{2}0]$. In phase II, two quadrupolar components are ordered; $\langle O_2^0\rangle$ and $\langle P_{xy}\rangle$. The zone-center component $\langle O_2^0\rangle$ is the same as in phase I but with an opposite sign, therefore the tetragonal strain mode also changes sign: $(a-c)/a>1$.[27] The $\langle P_{xy}\rangle$ components order within an antiferroquadrupolar arrangement propagated by the wave vector $\vec{q}=\vec{k}_1+\vec{k}_2=[\frac{1}{2}\frac{1}{2}0]$. The existence of charge satellites associated with this new periodicity in the crystal has been confirmed by x-ray diffraction experiments in nonresonant conditions.[8,28]

The NdMg sample issues from the same single crystalline ingot, processed with the Bridgman technique, as the sample used in reference.[8] It is a slab of 3.5×2 mm^2 and 1 mm height with a {100} cleaved surface. In the absence of an applied magnetic field, three magnetic domains are present in the two magnetic phases. Table I summarizes the contribution of each domain to the expected magnetic and quadrupolar reflections.

B. Experimental conditions

The diffraction experiments were carried out at the ESRF-Grenoble on the ID20 beamline (see Ref. 29). In a first step, studies were performed using an orange ILL-cryostat which allows a base temperature of 1.7 K to be reached. This setup imposes a horizontal diffraction plane (π-incident polarization) and impedes azimuthal scans. The sample was oriented and mounted inside the cryostat so that the horizontal diffraction plane was defined by the direction [001] perpendicular to the crystal surface and the direction [100] within the crystal surface. The azimuthal reference vector was chosen parallel to this direction thus magnetic and quadrupolar satellites were all collected at zero azimuthal angle.

A second series of measurements with purpose to study the azimuthal dependence of the quadrupolar reflections was performed using a close-cycle refrigerator with a 12.6 K base temperature. The vertical diffraction plane (σ-incident polarization) was chosen and the sample oriented so that this plane was determined by the [001] (perpendicular to the surface) and the [100] (within the surface) directions. The azimuthal reference vector was again chosen parallel to the [100] direction: at $\Psi=0°$, $\vec{h}_0=(100)$ (see Fig. 2). For both experimental configurations, horizontal and vertical diffraction planes, only the $(00l)$ reflections are specular.

The polarization of the scattered beam was selected by rotating a Cu(220) crystal analyzer about the diffracted beam, angle η in the following. For instance, the σ' emergent polarization is selected for $\eta=0(180)°$ (the diffraction plane of the sample coincides with that of the crystal analyzer) and the π' one for $\eta=90°$ (the diffraction planes of the sample and the crystal analyzer are perpendicular).

The reflection intensities were determined by integrating the rocking curve scans through the reflection except for the energy scans for which the points are taken at the intensity maximum of the reflections. Before performing these energy scans, the position of the threshold was checked in the fluorescence spectra collected from the background signal at the

TABLE I. Contributions of the three magnetic domains to the observable magnetic and quadrupolar reflections in the two magnetic phases of NdMg for a diffraction plane defined by the $[h00]$ and $[00l]$ crystallographic directions.

Domain	Magnetic	Quadrupolar	Magnetic satellites	Quadrupolar satellites
		Phase I		
D_x	$\vec{k}_x=[\frac{1}{2}00]$, $\vec{m}_x=[100]$	$\vec{q}_x=[000]$, $\langle O_2^0\rangle$	$(\frac{h}{2}0l)$	
D_y	$\vec{k}_y=[0\frac{1}{2}0]$, $\vec{m}_y=[010]$	$\vec{q}_y=[000]$, $\langle O_2^0\rangle$		
D_z	$\vec{k}_z=[00\frac{1}{2}]$, $\vec{m}_z=[001]$	$\vec{q}_z=[000]$, $\langle O_2^0\rangle$	$(h0\frac{l}{2})$	
		Phase II		
D_{xy}	$\vec{k}_x=[\frac{1}{2}00]$, $\vec{m}_x=[\frac{1}{\sqrt{2}}00]$	$\vec{q}_{xy}=[\frac{1}{2}\frac{1}{2}0]$, $\langle P_{xy}\rangle$	$(\frac{h}{2}0l)$	
	$\vec{k}_y=[0\frac{1}{2}0]$, $\vec{m}_y=[0\frac{1}{\sqrt{2}}0]$			
D_{yz}	$\vec{k}_y=[0\frac{1}{2}0]$, $\vec{m}_y=[0\frac{1}{\sqrt{2}}0]$	$\vec{q}_{yz}=[0\frac{1}{2}\frac{1}{2}]$, $\langle P_{yz}\rangle$	$(h0\frac{l}{2})$	
	$\vec{k}_z=[00\frac{1}{2}]$, $\vec{m}_z=[00\frac{1}{\sqrt{2}}]$			
D_{zx}	$\vec{k}_z=[00\frac{1}{2}]$, $\vec{m}_z=[00\frac{1}{\sqrt{2}}]$	$\vec{q}_{zx}=[\frac{1}{2}0\frac{1}{2}]$, $\langle P_{zx}\rangle$	$(h0\frac{l}{2})$	$(\frac{h}{2}0\frac{l}{2})$
	$\vec{k}_x=[\frac{1}{2}00]$, $\vec{m}_x=[\frac{1}{\sqrt{2}}00]$		$(\frac{h}{2}0l)$	

position $(-1.2-0.1\ 2.7)$ in the reciprocal space. As expected, the fluorescence at the L_2 edge is twice as small as at the L_3 edge. The spectra reported in Figs. 3(b) and 3(d) are normalized to the total jump at the threshold for the L_2 edge and to the half jump for the L_3. The determination of the threshold position in the fluorescence spectrum is useful in order to compare experimental and calculated RXS spectra. To superpose the internal energy scale in the calculations with the experimental energy scale, the origin of the energy scale in the calculations is translated so that the position of the threshold (white line maximum) in the fluorescence and calculated (FDM or MST-MT) x-ray absorption near-edge structure (XANES) spectra coincides [see, for instance, Figs. 3(b) and 3(d)]. Obviously at the L_3 edge, the white line is not well measured, indeed one expects roughly similar white line intensities at both edges. Nonetheless the position of the L_3 threshold is accurately determined and within the experimental resolution, the L_3 and L_2 threshold positions are found in good consistency: $\Delta E_{L_{2,3}} \approx 514$ eV. It is worth noting that the same offset of the energy origin is found in the FDM and in the MST-MT calculations.

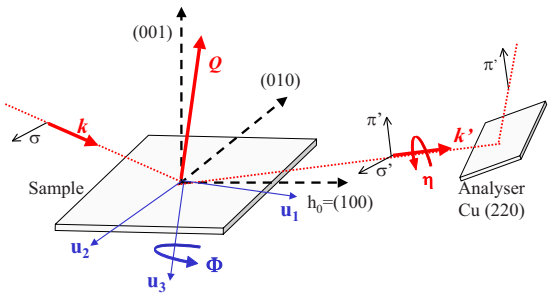

FIG. 2. (Color online) Scattering geometry for a vertical diffraction plane and incident σ linear polarization. $\vec{h}_0=(100)$ is the azimuthal reference vector. The polarization of the scattered beam is analyzed by rotating the Cu(220) crystal analyzer about the diffracted beam by the angle η. When the diffraction planes of the sample and the crystal analyzer coincide: $\eta=0°$ and the emergent σ' polarization is selected. On the contrary, the emergent π' is detected (case illustrated in the figure) when the diffraction planes of the sample and the crystal analyzer are perpendicular: $\eta=90°$.

The experimental conditions strongly limit the exploration of the reciprocal space for the studied compound. For the quadrupolar scattering, the two $(\pm\frac{1}{2}0\frac{5}{2})$ satellites were chosen because they are very close to the conditions for specular reflection. Therefore, the magnetic reflections were chosen in close vicinity in the reciprocal space with the aim to compare quadrupolar and magnetic resonant scattering. Four magnetic satellites with comparable magnetic form factors were measured: $(\frac{1}{2}02)$, $(\pm\frac{1}{2}03)$, and $(00\frac{5}{2})$. The three magnetic domains are associated to the tetragonal deformation and result in three intensity peaks close in position. The angular experimental resolution at the Nd $L_{2,3}$ edges does not allow us to measure them separately. Therefore, no information concerning the population of the magnetic domain that contributes to the quadrupolar satellites is accessible. For the study of the azimuthal dependence, it is necessary to take notice of this domain distribution. Actually at each azimuth the incident beam illuminates different surfaces of the sample. This can be considered as exploring different samples with different domain distributions. To avoid artifacts arising from this effect, the rotated, σ-π', and unrotated, σ-σ', integrated intensities measured at the maximum of the quadrupolar resonance $(E_i=6724.5$ eV) were normalized to the unrotated nonresonant signal measured at $E_i=6710$ eV.

III. *AB INITIO* SIMULATIONS OF THE SPECTRA

A. Cross section and structure factor

The main quantitative features of absorption and resonant diffraction are the cross section σ and, respectively, the structure factor $F(\vec{Q},\omega)$, both normalized with respect to the unit cell,

$$\sigma(\omega) = 4\pi^2\alpha\hbar\omega\sum_j \sum_{f,g} |\langle\psi_f|\hat{O}|\psi_g^{(j)}\rangle|^2 \delta[\hbar\omega - (E_f - E_g^{(j)})], \quad (1)$$

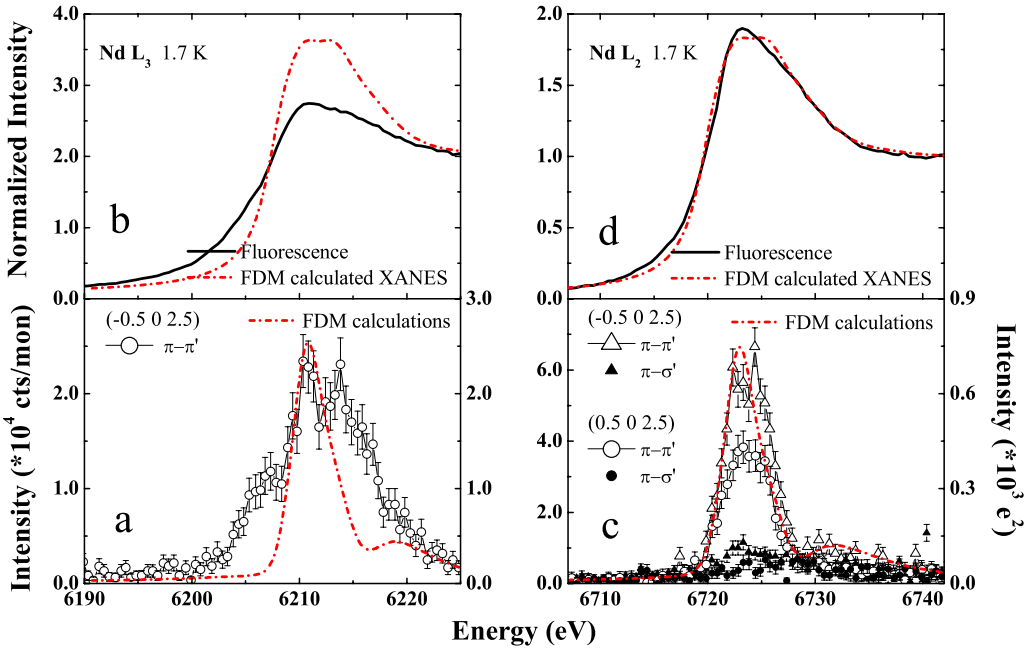

FIG. 3. (Color online) $T=1.7$ K. Lower parts, (a) and (c), show the energy scans performed at the positions of the quadrupolar satellites: $(\pm\frac{1}{2}0\frac{5}{2})$, in the π-π' (open symbols) and π-σ' (full symbols) channels at the L_3 (a) and L_2 (c) edges of Nd. The experimental spectra (solid line) are compared with the simulations (dash dot line) performed within the FDM framework for $\Psi=0°$. The upper parts [(b) and (d)] report the experimental fluorescence spectrum (solid line) and the calculated XANES (dash dot line) at the L_3 (b) and L_2 (d) edges, respectively.

$$F(\vec{Q},\omega) \propto \sum_j e^{i\vec{Q}\vec{R}_j}[f_{0j} + if_{mj} + f'_j(\omega) + if''_j(\omega)] \qquad (2)$$

with

$$f^*_j(\omega) = \frac{m_e}{\hbar^2}\sum_{f,g} \frac{(E_f - E_g^{(j)})^2 \langle \psi_g^{(j)}|\hat{O}^\dagger_{out}|\psi_f\rangle\langle\psi_f|\hat{O}_{in}|\psi_g^{(j)}\rangle}{\hbar\omega - (E_f - E_g^{(j)}) + i\frac{\Gamma_f}{2}}. \qquad (3)$$

Here α is the fine-structure constant, m_e the electron mass, and $\hbar\omega$ the photon energy. E_g and E_f are the energies of the ground state $\psi_g^{(j)}$ and photoexcited state ψ_f, respectively, with j the index of the atom in the unit cell. The final state ψ_f is an unoccupied state above the Fermi energy E_F, where for simplicity we omit its j index. ψ_f is calculated assuming the excited electronic configuration of the absorbing atom. $\vec{Q}$ is the diffraction vector and $\vec{R_j}$ is the position vector of the atom j in the unit cell. Γ is the inverse of the sum of the final state and the core-hole lifetime, and thus depends on the choice of the absorber. The scattering amplitudes in Eq. (2) are the nonresonant energy-independent spherical Thomson term, f_{0j}, the nonresonant anisotropic magnetic term, f_{mj}, and the complex resonant contribution, $f'_j(\omega)+if''_j(\omega)$, respectively.

The electron-photon interaction is described classically by the means of the field operator $\hat{O}$. In the x-ray regime, the magnetic part of the electromagnetic field can be neglected and the remaining electric part is satisfactorily described by the first two terms of the multipolar expansion,

$$\hat{O} = \vec{\epsilon}\cdot\vec{r}\left(1 + \frac{1}{2}i\vec{k}\cdot\vec{r}\right), \qquad (4)$$

where $\vec{r}$ is the position from the absorbing atom, $\vec{\epsilon}$ the polarization of the photon, and $\vec{k}$ its corresponding wave vector. The first term of this expansion is responsible for the so-called electric dipole E1 transitions whereas the second one induces the electric quadrupole E2 ones.

B. Tensorial approach

Absorption and RXS are strongly related phenomena, as they depend on the same transition matrix and obey to the same ℓ and m quantum-numbers' selection rules. Because RXS is very sensitive to the anisotropy of the scattering, the possibility to combine incoming and outgoing polarizations and to choose specific reflections make this technique a valuable method to probe the physical mechanisms that cause the anisotropy. For instance, RXS allows the observation of the so-called forbidden reflections that cannot be observed within the isotropic Thomson diffraction. At the absorption edges, the nonresonant Thomson and magnetic scattering amplitudes in Eq. (2) become quantitatively negligible compared to the anomalous scattering amplitude, nonetheless in the present calculations the nonresonant spherical Thomson and magnetic contributions are taken into account. On the other hand, the nonspherical Thomson term that gives rise to the nonresonant multipolar scattering[30] is neglected.

As involved phenomena are anisotropic, both the physical origin and the azimuthal dependence of the reflections can be understood in terms of a tensorial algebra. In the current section, for the sake of simplicity, we restrain the multipolar expansion of the field operator to the dipolar contribution: $\hat{O}=\vec{\epsilon}\cdot\vec{r}$. Consequently, the resonant atomic scattering amplitude can be rewritten as

TABLE II. Positions in the chemical unit cell of the equivalent atoms. The third column lists the symmetry operations that link these atoms to the central one ($j=0$). E stands for the identity, C_{4z} means a $\pi/2$ rotation around the Oz axis, and T stands for time reversal.

j	$\vec{R}_j$	Op. sym.
1	0 0 0	E
2	1 0 0	C_{4z}
3	0 1 0	TC_{4z}
4	1 1 0	TE

$$f_j^*(\omega) = \frac{m_e}{\hbar^2}\int_{E_F}^{\infty} dE_f \frac{(E_f - E_g^{(j)})^2}{\hbar\omega - (E_f - E_g^{(j)}) + i^{\Gamma_f/2}} \times \sum_{\alpha\beta} \epsilon_\alpha^\dagger \epsilon_\beta D_{\alpha\beta}^{(j)}(\hbar\omega = E_f - E_g^{(j)}). \quad (5)$$

$D_{\alpha\beta}^{(j)}(\alpha,\beta \in \{x,y,z\})$ are the energy-dependent components of the cartesian, dipolar, atomic tensor describing the resonant process,

$$D_{\alpha\beta}^{(j)}(\hbar\omega = E_f - E_g^{(j)}) = \sum_{f,g} \langle \psi_g^{(j)} | r_\alpha | \psi_f \rangle \langle \psi_f | r_\beta | \psi_g^{(j)} \rangle. \quad (6)$$

The f index accounts for the final states of same energy E_f. The atomic tensor D is a tensor of rank 2 and has the form of a Hermitian matrix: $D_{\alpha\beta}=D_{\beta\alpha}^*$. The components can be linked to observables. The isotropic contribution to the scattering at the resonance is given by the trace of the tensor (a rotational invariant) normalized by a $\sqrt{3}$ factor. The term $D_{yz}-D_{zy}=i\sqrt{2}l_x$ (*idem* for circular permutations) where l_x is the projection of the atomic orbital momentum *per* energy unit on the Ox axis. The atomic tensor D is invariant in the symmetry operations of the magnetic point group of the atomic site. In periodic structures, it is more convenient to deal with the crystal tensor $\mathcal{D}$ given by

$$\mathcal{D}_{\alpha\beta} = \sum_{j \in \text{unit cell}} D_{\alpha\beta}^{(j)}. \quad (7)$$

The symmetry of $\mathcal{D}$ is determined by the space group of the crystal. The crystal tensor $\mathcal{D}$ is used, for instance, in the calculation of the absorption. To describe the diffraction, it is useful to introduce the structure factor tensor given by

$$\mathcal{D}_{\alpha\beta}(\vec{Q}) = \sum_j e^{i\vec{Q}\vec{R}_j} D_{\alpha\beta}^{(j)} = \sum_{\text{nonequiv}} \sum_{\text{equiv}} e^{i\vec{Q}\vec{R}_j} \text{sym}(D_{\alpha\beta}), \quad (8)$$

where $\vec{Q}=(hkl)$ is the scattering vector. FDMNES uses symmetries to reduce the computation time: only the tensors of the nonequivalent atoms are calculated, then symmetry operations are use to deduce those of the other atoms. Table II shows for instance the symmetry operations that rely, in the unit cell of NdMg, the atoms of the plane parallel to the magnetic moments.

Let us consider the magnetic domain where the spins lie in the plane xOy. The corresponding magnetic point group is $m'm'm$, leading to the following form for the atomic tensor in the crystal basis set:

$$D = \begin{pmatrix} a & c & id \\ c & a & -id \\ -id & id & b \end{pmatrix}. \quad (9)$$

The energy-dependent components: a, b, c, and d, are real numbers. We can note, for instance, that, as $D_{xy}-D_{yx}=0$, the atomic orbital momentum along the Oz axis is zero. Equations (8) and (9) and the symmetry information given in Table II lead to the following form for the crystal tensor:

$$\mathcal{D} = 4\begin{pmatrix} a & 0 & 0 \\ 0 & a & 0 \\ 0 & 0 & b \end{pmatrix}. \quad (10)$$

In the same way, the following forms are obtained for the amplitudes $A^{(j)}$ for the $(\frac{h}{2}00)$ and the $(\frac{h}{2}\frac{k}{2}0)$ reflections:

$$A_{(h/2)00}^{(j)} \propto \epsilon_{out}^\dagger \begin{pmatrix} 0 & 0 & 0 \\ 0 & 0 & -4id \\ 0 & 4id & 0 \end{pmatrix} \epsilon_{in}, \quad (11)$$

$$A_{(h/2)(k/2)0}^{(j)} \propto \epsilon_{out}^\dagger \begin{pmatrix} 0 & 4c & 0 \\ 4c & 0 & 0 \\ 0 & 0 & 0 \end{pmatrix} \epsilon_{in}. \quad (12)$$

We draw the attention upon the fact that Eqs. (11) and (12) involve only one value among the atomic tensor's elements. This implies that the global shape of the angular dependence is energy independent. The angular dependence reckons on the energy via an energy-dependent multiplicative factor.

Note that these results, obtained with a cartesian tensor algebra, can be reformulated in terms of spherical tensors in the spirit of Blume's[31] formula. The two approaches are completely equivalent and lead to the same results. It is worth noting that the third contribution $(\vec{\epsilon'}\cdot\vec{z}_j)(\vec{\epsilon}\cdot\vec{z}_j)$ in the expression of the resonant scattering amplitude given by Hannon *et al.* (Eq. 3 in Ref. 31) and reformulated latter on by Hill and McMorrow,[32] leads to the same azimuthal dependence for the resonant $(\frac{1}{2}0\frac{5}{2})$ reflection as the present calculations.

The components of the tensor in Eq. (11) being purely imaginary, the $(\frac{h}{2}00)$ reflections are thus magnetic. In Eq. (12), the components being purely real, the reflections at the $(\frac{h}{2}\frac{k}{2}0)$ nodes are electrical. We note that the class of $(0\frac{h}{2}0)$ reflections is equivalent to the $(\frac{h}{2}00)$ ones as the site has the C_{4z} symmetry. Therefore, in order to obtain its tensorial amplitude it is enough to refer to Eq. (11) and perform the corresponding symmetries.

The tensorial approach allows us understanding the extinction of certain reflections due to a specific combination between the incoming and the outgoing polarizations. For instance, the amplitude of the magnetic $(\frac{h}{2}00)$ reflections in the $\sigma-\sigma'$ configuration give (see Eq. (11))

$$(0 \quad -\sin\Psi \quad -\cos\Psi)\begin{pmatrix}0 & 0 & 0\\ 0 & 0 & -4id\\ 0 & 4id & 0\end{pmatrix}\begin{pmatrix}0\\ -\sin\Psi\\ -\cos\Psi\end{pmatrix}=0,$$

where Ψ is the azimuthal angle. The experiment confirms the extinction of this specific reflection. The same reflection in the σ-π' configuration is isotropic with respect to the azimuthal angle,

$$(\sin\theta \quad \cos\theta\cos\Psi \quad -\cos\theta\sin\Psi)\begin{pmatrix}0 & 0 & 0\\ 0 & 0 & -4id\\ 0 & 4id & 0\end{pmatrix}\times\begin{pmatrix}0\\ -\sin\Psi\\ -\cos\Psi\end{pmatrix}=4id\cos\theta,$$

where θ is the Bragg angle.

Please note that the scattering tensor being Hermitian, the σ-π' polarization configuration yields the same results as the π-σ' one. In the same way, we checked the π periodicity of the quadrupolar $(\frac{h}{2}\frac{k}{2}0)$ σ-π' reflections,

$$(\sin\theta\cos\alpha-\cos\theta\sin\alpha\cos\Psi \quad \sin\theta\sin\alpha+\cos\theta\cos\alpha\cos\Psi \quad -\cos\theta\sin\Psi),$$

$$\begin{pmatrix}0 & 4c & 0\\ 4c & 0 & 0\\ 0 & 0 & 0\end{pmatrix}\begin{pmatrix}\sin\Psi\sin\alpha\\ -\sin\Psi\cos\alpha\\ -\cos\Psi\end{pmatrix}=c(-4\cos 2\alpha\sin\Psi+\cos\theta\sin 2\alpha\sin 2\Psi)$$

with $\alpha=\arctan(h/k)$

The calculations described above (diffraction amplitudes, crystal tensor, and azimuthal dependence) are implemented in the FDMNES code and performed automatically. In comparison to the analytical calculations, the numerical ones provide the exact value of the atomic tensor components $(a,\ b,\ c,\ d)$, thus permitting a quantitative analysis of the angular dependence.

C. About the calculation code

In NdMg, the final states of the dominant E1 electric dipole transitions at the Nd $L_{2,3}$ edges are the $5d$ conduction band states. Therefore a monoelectronic approach is well adapted to simulate the experimental spectra. When the final states are localized as, for instance, the $4f$ final states of the E2 transitions a correct description requires a multielectronic approach. We will show in the following that nonetheless a monoelectronic approach is able to predict the right position in energy for the E2 transitions.

The *ab initio* simulations of the RXS spectra have been performed using the FDMNES package.[24–26] In the FDMNES code, the calculations are carried out in the real space using clusters built around each nonequivalent absorbing atom and independently for each nonequivalent absorber. As for other monoelectronic approaches, the main difficulty is the calculation of the final states. Two methods are available to achieve these final-state calculations: the FDM and the MST, in the limit of the MT approximation. The MT approximation assumes a crystal potential of spherical symmetry around the atoms and constant in the remaining space. Recently the code has been implemented with a self-consistent procedure that is described in Ref. 26. The self-consistent procedure is developed in three steps. First, the electronic structure is solved within a ground-state description, i.e., without considering the core hole. This typically takes some tenths of cycles to obey the convergence criterion linked to the total energy of the cluster. In this step, calculations are performed in the MST-MT framework, thus by the nature of the MT approximation, at the beginning of each iteration the nonsphericity which may result from the previous calculation is eliminated. Second, once the ground-state electronic structure has been determined, a new potential is calculated that includes the core-hole effects and the associated screening and one solves either the Schrödinger or the Dirac equation, using the MST-MT or the FDM method. The same cluster radius is kept in the two steps. Third, by using the value of the Fermi level, determined in the first step, the structure factor and the absorption signal, according to Eqs. (1) and (2) are calculated. The convolution parameter Γ is the same in the two cases. We note that we can perform a nonself-consistent calculation by skipping the first step and performing directly the second and the third one.

The FDM is a full-potential method that does not introduce any approximation on the shape of the potential. The cluster potential is calculated in every point of the space grid by superposing the self-consistent atomic potentials. Subsequently, the radial Schrödinger equation is discretized and solved point by point. This makes FDM an ideal tool for calculations on materials where the nonsphericity plays an important role. An increased CPU time and virtual memory are however the price to pay for the gain in accuracy. At present, the limited computer resources do not allow including the spin-orbit coupling into the FDM framework within a

reasonable calculation time (a couple of months, on a SGI ALTIX 450 machine). Therefore, for the time being, we are unable to run a calculation that takes into consideration simultaneously the distortion of the electronic cloud and the spin-orbit coupling in the final states. Consequently it was chosen to perform simulations within the FDM framework for the electric quadrupolar reflections and within the MST-MT framework for the magnetic reflections.

In the case of the magnetic reflections, the magnetic effects are treated through a relativistic extension of the Schrödinger equation built without any approximation from the Dirac equation. Magnetic effects are treated rigorously as the spin-orbit coupling is taken into account for both the core state and the final ones. The double-$\boldsymbol{k}$ spin arrangement in phase II of NdMg is explicitly given as input information. In this approach, no attempt was made to account for the nonsphericity of the $4f$ electronic distribution and no description of the antiferroquadrupolar ordering was given. The MST calculations of the XANES and RXS spectra were performed on a cluster of radius 6 Å containing 27 atoms.

The antiferroquadrupolar ordering of the $4f$ electric quadrupolar moments introduces a periodic perturbation of the potential that affects the $5d$ finals states and gives rise to the resonant scattering at the $(\frac{h}{2}0\frac{l}{2})$ nodes in the reciprocal space. The existence of the $4f$ electric quadrupolar moment should be described through a convenient breaking of the $4f$ orbital symmetry. As long as the FDM calculations are concerned, the degeneracy is removed by imposing a specific extra population to a $4f$ orbital provided it possesses an axial symmetry along the local direction of the quantization axis defined by the local magnetic moment. It is the Coulomb repulsion of this aspherical extra electric charge which breaks the local symmetry and splits the $5d$ levels. To obey to the axial symmetry constraints, we chose the $m_{4f}=0$ orbital and rotated it to align it to the direction of the spins (see Fig. 1). Calculations were run on a cluster of radius 4 Å, centered on the absorbing atom and containing the first two neighboring shells, i.e., 15 atoms. An extra population of 0.15 electrons was imposed to the $m_{4f}=0$ orbital but no magnetic information was introduced in the calculations.

IV. RESULTS

A. Quadrupolar scattering

Figures 3(a) and 3(b) show the energy spectra of the $(\pm\frac{1}{2}0\frac{5}{2})$ quadrupolar satellites in phase II (1.7 K) at the Nd $L_{2,3}$ absorption edges. In the π-π' channel, the quadrupolar scattering presents a single-peak resonant structure centered around ≈6724 and ≈6212 eV for the L_2 and L_3 edges, respectively. As observed for the $(-\frac{1}{2}0\frac{5}{2})$ reflection, at the L_3 edge, the resonant enhancement is at least three times smaller than at the L_2 edge. The polarization of the scattered beam is clearly π' and the weak intensity in the π-σ' channel measures the leakage from the π-π' channel. The $(\frac{1}{2}0\frac{5}{2})$ reflection has a smaller intensity than the equivalent at $(-\frac{1}{2}0\frac{5}{2})$. A similar effect is observed for the off-specular magnetic reflections between reflections with positive and negative h index. This is ascribed to a slight misalignment of the crystal surface.

Experiments with σ-incident polarization were performed only at the L_2 edge with the main purpose of studying the azimuthal dependence. They were carried out with a very different experimental setup, therefore only the shape and the position in energy of the resonance can be compared with the previous π-incident experiments. A clear resonant enhancement is observed in the σ-π' channel as shown in Fig. 4(a). Its position in energy and its shape are quite similar to those observed in the π-π' channel. In the σ-σ' channel, a significant signal is also measured, whose energy dependence is reminiscent of a nonresonant process.

Figure 3 compares also the experimental spectra to the *ab initio* simulations within the FDM full-potential framework. The simulations of the quadrupolar scattering have been carried out in the π-π' geometry for the azimuthal angle $\Psi=0°$. In this approach, the magnetic aspect is not accounted for, i.e., one supposes a nonmagnetic compound and the orbital symmetry breaking of the $4f$ electronic cloud is accounted for by imposing a specific extra population on one $4f$ orbital. The curves presented in Figs. 3 and 4 have been calculated with an extra population of 0.15 electrons on the $m_{4f}=0$ orbital. Increasing (decreasing) this population increases (decreases) the intensity of the quadrupolar satellite energy spectra but affects neither the shape of the spectra nor the intensity ratio between the $L_{2,3}$ edges. We note that the discrepancy between the calculated and experimental white line intensities at the L_3 edge is ascribed to the bad measurement of the white line in the fluorescence scan. At the L_2 edge, calculated XANES and experimental fluorescence spectra are fully consistent.

The calculated intensities in the π-π' channel for the $(\pm\frac{1}{2}0\frac{5}{2})$ quadrupolar satellites present the same energy dependence at both edges. A main resonance, peaking at 6723.2 and 6211 eV for the L_2 and L_3 edges, respectively, is followed by a much smaller peak located at ≈8–9 eV above in energy (see Fig. 3). The position and the shape of the main resonant peak coincide well with the experimental spectra. The experimental resolution is not sufficient to draw any conclusion about the existence of the second peak at higher energy. A very small scattering (not shown) is calculated in the π-σ' geometry in agreement with the experimental observations. However, contrary to the observations, the calculated resonant enhancement is much larger at the L_3 than at the L_2 edge.

Figure 4(b) shows the polarization dependence of the scattered beam at the $(\frac{1}{2}0\frac{5}{2})$ and (002) nodes for three different incident photon energies: 6710, 6721, and 6724.5 eV for $0\leq\eta\leq180°$. The integrated intensities were fitted using the expression: $I(\eta)\propto[1+P_1\cos(2\eta)+P_2\sin(2\eta)]$, for the transmission function of an idealized linear polarization analyzer [Eq. 1 in Ref. 33] where P_1 and P_2 are the Stokes parameters. The fits and the resulting Stokes parameters are reported in Fig. 4(b) and in Table III, respectively. The (002) intensity decreases when approaching the absorption edge but keeps its maximum amplitude in the σ-σ' channel independently of the incident photon energy. The behavior of this spherical Thomson scattering [term f_{0j} in Eq. (2)] is well reproduced by the FDM simulations. Below the edge at $E_i=6710$ eV, the intensity of the $(\frac{1}{2}0\frac{5}{2})$ reflection that results from the nonspherical Thomson scattering presents also a

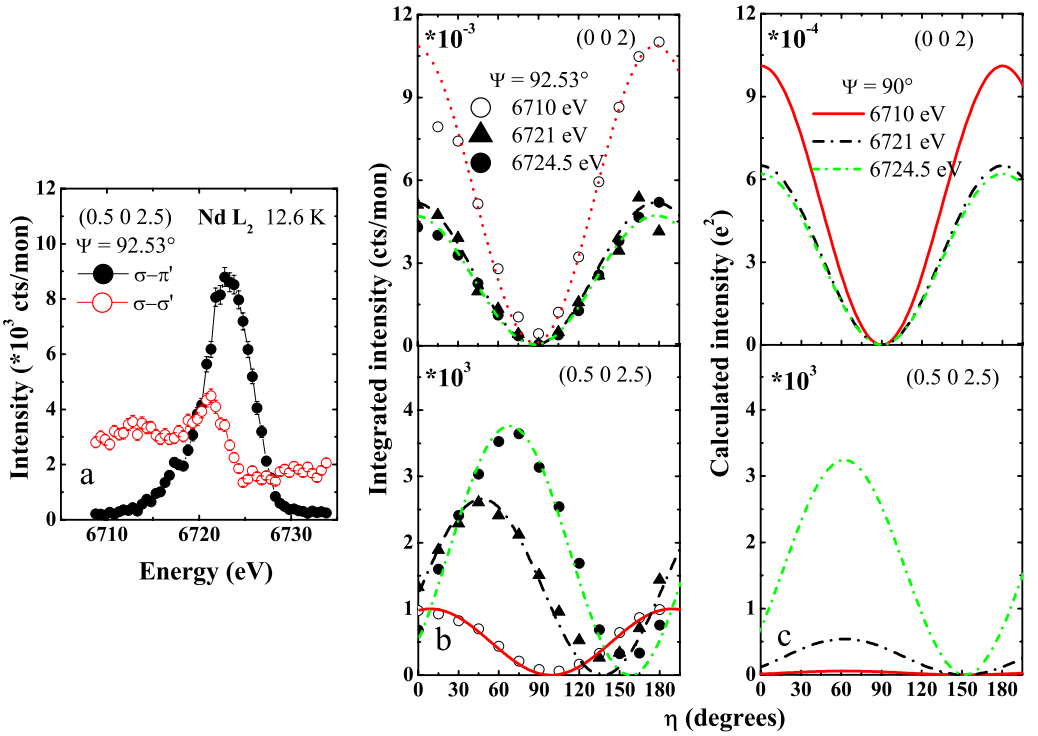

FIG. 4. (Color online) (a) Nd L_2 edge, energy scan of the $(\frac{1}{2}0\frac{5}{2})$ quadrupolar satellite in the σ-π' and σ-σ' channels at azimuth Ψ =92.53°. (b) Dependence of the degree of linear polarization of the diffracted beam for the same $(\frac{1}{2}0\frac{5}{2})$ quadrupolar satellite as a function of the incident photon energy. This dependence is compared to that of the (002) main charge reflection. The lines represent the fits to the transmission function of an idealized linear polarization analyzer (see text). The values of the Stokes parameters are given in Table III. The σ' emergent polarization is selected for η=0 and 180° and the π' one for η=90°. (c) Simulations of the polarization dependence of the $(\frac{1}{2}0\frac{5}{2})$ and (002) reflections within the FDM full-potential framework. Calculations were performed for an azimuthal angle Ψ=90°. They account for the anomalous phenomena and the spherical Thomson terms but not for the nonspherical Thomson term that gives rise to the nonresonant multipolar scattering.

maximum in the σ-σ' configuration. When approaching the L_2 edge, the maximum of the intensity progressively shifts toward $\eta \approx 60°$ and increases by a factor 3, in agreement with a resonant process. The FDM simulations of the $(\frac{1}{2}0\frac{5}{2})$ reflection predict a squared sinusoidal-like behavior of the intensity with η whose minima depend on the azimuthal angle Ψ, in present calculations Ψ =90°. In Fig. 4(c), the calculated curve reproduces quite well the experimental behavior at the resonance (E_i=6724.5 eV). The discrepancy observed between experiment and calculation at E_i=6710 and 6721 eV illustrates the fact that the nonspherical Thomson term is neglected in the FDM simulations. This confirms that the experimental signal at 6724.5 eV is purely resonant in both, the σ-π' and σ-σ' channels while it essentially arises from the nonspherical Thomson scattering at 6710 eV. The dependence observed at 6721 eV suggests that close to the edge, nonspherical Thomson and resonant scatterings interfere in the σ-σ' configuration.

TABLE III. Stokes parameter used to fit the dependence of the degrees of σ' and π' polarization of the diffracted beam for the (002) lattice reflection and the $(\frac{1}{2}0\frac{5}{2})$ quadrupolar satellite, reported in Fig. 4.

Energy (eV)	Reflection	P_1	P_2
	(200)	0.98 ± 0.05	−0.09 ± 0.05
6710	$(\frac{1}{2}0\frac{5}{2})$	0.95 ± 0.05	+0.31 ± 0.05
	(200)	0.98 ± 0.05	−0.09 ± 0.05
6721	$(\frac{1}{2}0\frac{5}{2})$	−0.08 ± 0.05	0.99 ± 0.05
	(200)	0.98 ± 0.05	−0.09 ± 0.05
6725	$(\frac{1}{2}0\frac{5}{2})$	−0.72 ± 0.05	0.69 ± 0.05

The azimuthal dependence of the $(\frac{1}{2}0\frac{5}{2})$ integrated intensity was measured in both the σ-π' and σ-σ' channels for an incident photon energy of E_i=6724.5 eV and in the σ-σ' channel only for the nonresonant signal at E_i=6710 eV. The azimuthal angle dependence of the normalized signals is reported in Fig. 5. The σ-π' signal exhibits a clear maximum around Ψ=90°. Though the unrotated signal keeps a much smaller intensity a maximum occurs at the same azimuth. Figure 5 shows also the *ab initio* calculated variation of the resonant scattering at the $(\frac{1}{2}0\frac{5}{2})$ position as a function of the azimuthal angle. In both channels, σ-π' and σ-σ', the experimental azimuthal dependence is completely consistent with the calculations. This agreement validates the initial choice made to break the 4*f* symmetry.

B. Magnetic scattering

Consistent with the magnetic structure of NdMg in phase II, measurements show that the magnetic scattering occurs

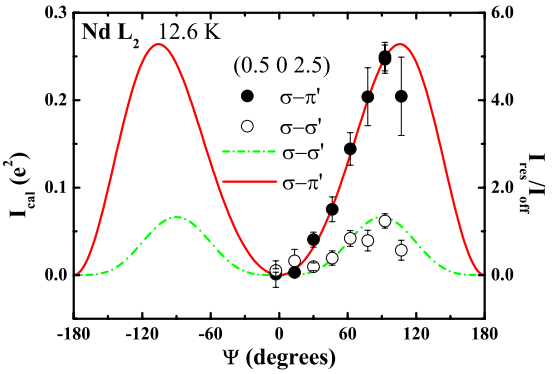

FIG. 5. (Color online) Nd L_2 edge, azimuthal dependence of the $(\frac{1}{2}0\frac{5}{2})$ reflection in the σ-π' and σ-σ' channels. Filled and open circles represent the experimental integrated intensities normalized to the unrotated nonresonant intensity (E_i=6710 eV). The lines represent the azimuthal dependence calculated in the σ-π' (full line) and σ-σ' (dashed line) channels within the FDM full-potential framework.

only in the rotated π-σ' or σ-π' channels. Figure 6 reports the energy scans at the $L_{2,3}$ edges for the magnetic satellites with a π-incident polarization. The structure of the resonant spectra apparently depends on the edge and on the specular or off-specular character of the reflections.

At the L_3 edge, all resonant spectra present a wide structure peaking at E_0=6208 eV, the tabulated electron binding energy (Ref. 34). A much smaller structure is also observed at ≈6214 eV. Below the edge, however, the structure differs between specular and off-specular reflections. While at ≈6205 eV, the $(00\frac{5}{2})$ specular reflection shows a third peak, larger than the one at E_0, a clear minimum is observed at the same energy for the $(\frac{1}{2}02)$ off-specular one. For this last reflection a third peak is observed at ≈6202 eV, and a non-negligible intensity is still measured far below the edge.

At the L_2 edge, for all the magnetic reflections, one main peak is again observed at the binding energy, E_0=6722 eV, followed by a second one at ≈6727 eV. Quite similarly to the L_3 edge, the off-specular reflection $(-\frac{1}{2}03)$ (or the $(\frac{1}{2}03)$ not shown here) presents, below the edge, a pronounced structure around 6715 eV and keeps far below the edge a measurable intensity, of the same order as the L_3 intensity. Conversely the $(00\frac{5}{2})$ intensity progressively decreases and vanishes below the edge. For this $(00\frac{5}{2})$ satellite an energy scan, not shown here, performed at the L_2 with an incident σ polarization and at Ψ=92.53° presents exactly the same shape.

The simulations of the magnetic reflections were carried out within the MST-MT approach that allows including the spin-orbit coupling. The magnetic energy spectra have been calculated in the π-σ' and π-π' configurations for two values of the azimuthal angle Ψ=0 and 45°. Also two values for the cutoff energy have been used, the self-consistent Fermi-energy value and a value shifted down by 1.2 eV. We will explain later the choice of these two energies. In agreement with the magnetic structure in phase II, no magnetic signal is calculated in the π-π' channel. The π-σ' calculated spectra with the two different cutoff energies at Ψ=0° are reported in Fig. 6. Energy spectra present mainly a two-peak structure with a main peak at the binding energy E_0 and a smaller one located 4 eV above. The same calculations for Ψ=45° reveal a strong effect of the azimuth on the off-specular reflection intensities. As illustrated in Fig. 7 for the $(\frac{1}{2}02)$ reflection,

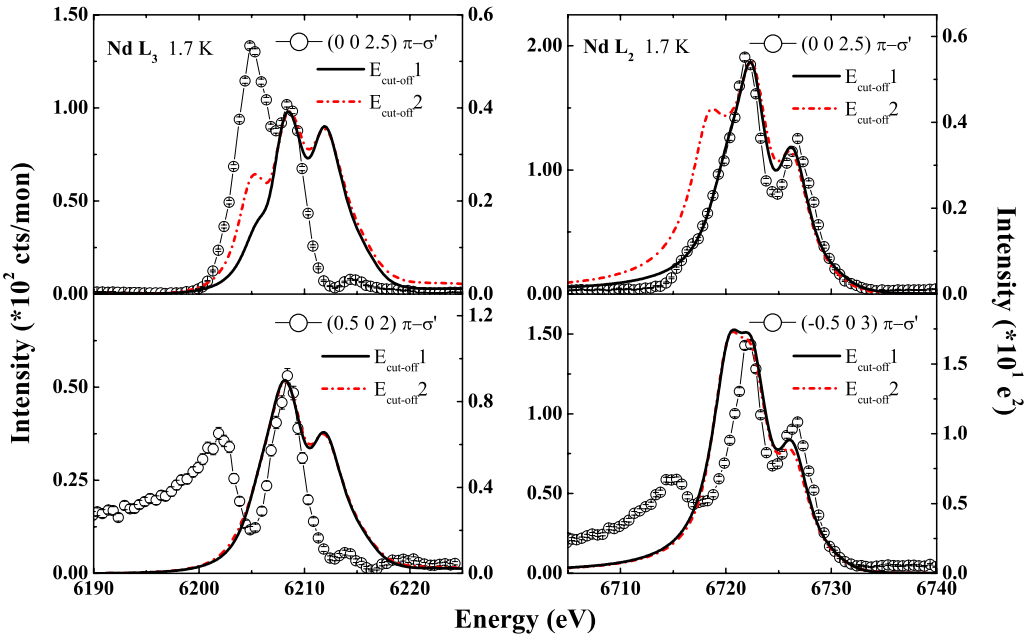

FIG. 6. (Color online) Energy scans through the Nd $L_{2,3}$ edges on the magnetic scattering at the $(00\frac{5}{2})$, $(-\frac{1}{2}03)$, and $(\frac{1}{2}02)$ nodes in the π-σ' channel. Experimental spectra are compared to simulations carried out within the MST-MT framework including the spin-orbit coupling. Full lines represent the simulations obtained using the value of the Fermi energy calculated self-consistently as cutoff energy ($E_{cutoff}1$), dash dot lines those obtained using a value of the cutoff energy, ($E_{cutoff}2$), shifted down by 1.2 eV from the previous value. The spectra shown in the figure were all calculated assuming Ψ=0°.

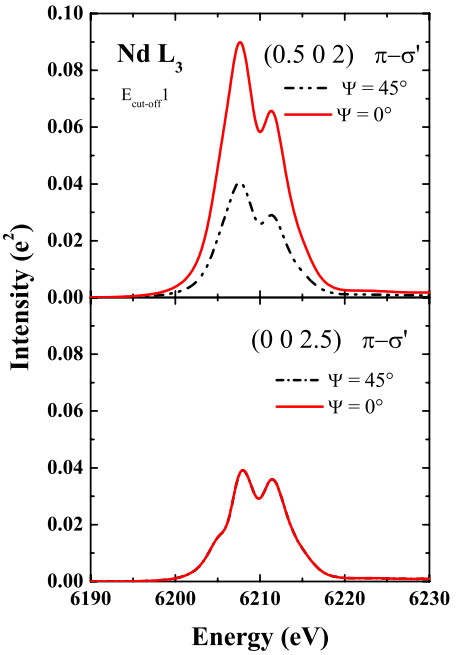

FIG. 7. (Color online) Nd L_3: azimuthal effects in the energy spectra of the resonant magnetic scattering for specular $(00\frac{5}{2})$ and off-specular $(\frac{1}{2}02)$ reflections predicted within the self-consistent MST-MT approach including the spin-orbit coupling. The cutoff energy is the calculated Fermi level.

the intensity at $\Psi=0°$ is twice as large as at $\Psi=45°$. For the specular reflection due to the symmetry of the magnetic propagation vector no azimuthal effect is predicted.

The calculations reproduce rather well the main features of the experimental spectra above the edge (see Fig. 6). In particular, the positions in energy of the peaks in the simulations compare well with the experimental ones. At the L_2 edge, the relative intensities between the two peaks is also well reproduced. At the L_3 edge, however, the second peak is predicted with an intensity far larger than observed experimentally. Such a discrepancy could be due to absorption effects not taken into account in the calculations.

At the L_3 edge, the spectrum calculated with the self-consistent value of E_F as energy cutoff ($E_{cutoff}1$) for the $(00\frac{5}{2})$ specular reflection presents a small bump at the position where the third peak is observed experimentally ($\approx$6205 eV). In the calculations, this bump is unambiguously assigned to the E2 electric quadrupole transitions. Calculations were performed using a lower value of the energy cutoff, $E_{cutoff}2$, value shifted down by 1.2 eV from $E_{cutoff}1$. Note that when multielectronic effects are present the concept of Fermi level loses its significance and a best description could be obtained by adjusting the cutoff energy. This is a reasonable procedure in the present case. While for the off-specular reflections, no change occurs in the structure of the spectra, the peak due to E2 transitions is clearly resolved at the L_3 and L_2 edges in the specular case. It is known that monoelectronic approaches are not adapted to describe strongly correlated electrons, nonetheless the consistency between calculations and experimental observations allows to definitively ascribe the peak observed at 6205 eV in the L_3 spectrum of the $(00\frac{5}{2})$ reflection to the E2 electric quadrupole transitions.

The non-negligible intensity measured far below the $L_{2,3}$ edges for the off-specular reflections is due to the nonresonant magnetic scattering. A nonresonant magnetic scattering measurable only at the off-specular positions could be explained by a strong imbalance in the magnetic domain population. According to Table I, domains D_{xy} and D_{zx} contribute to the off-specular reflections and domains D_{yz} and D_{zx} to the specular ones. Actually the domain distribution remains unknown and it is not likely that the probed volume presents the ideal domain equipartition in zero applied magnetic field. If for any reason, the D_{xy} domain is strongly favored at the crystal surface, the nonresonant scattering arising from this domain will dominate that from the D_{zx} and D_{yz} domains. This will lead to a larger scattered intensity at the off-specular positions. The fact that at the resonance, the off-specular scattering becomes smaller than the specular scattering can be explained by the conjoint effects of the crystal misalignment and the absorption. Unfortunately without applying a magnetic field, it is impossible to access the domain distribution at the probed surface. Nonetheless an imbalance in the domain population, e.g., a favored D_{xy} domain to the detriment of the D_{zx} and D_{yz} domains, is consistent with the weakness of the resonant quadrupolar scattering compared to the magnetic scattering. Indeed the experimental conditions limit the access to only the D_{zx} domain for the quadrupolar satellites. The origin of the broad structure observed at both edges at $\approx$6–7 eV below the E_0 peak in the energy spectra for the off-specular reflections remain unclear.

To treat rigorously the magnetic problem it is necessary to account for the spin-orbit coupling. We performed this in the MST-MT model only, as it would have not been tractable within the FDM. In the MST frame, the description of the magnetic arrangement is an input information in the calculations but no information concerning the antiferroquadrupolar arrangement is given. Nonetheless MST calculations predict in the π-π' channel a scattered signal at the $(\frac{h}{2}0\frac{l}{2})$ quadrupolar nodes. The magnetic scattering that occurs only in the rotated π-σ' or σ-π' channels is forbidden at these nodes. Such a result is quite unexpected as in the self-consistent procedure the MT approximation naturally erases any kind of asphericity of the electric potential resulting from the previous iterations. When the spin-orbit coupling is not introduced, the MST-MT calculations, both self-consistent and nonself-consistent, do not predict any scattering at the quadrupolar nodes. One thus ascribes the emergence of this scattering to the spin orbit, which by coupling the magnetic moment and the $4f$ electronic distribution allows predicting these nonspherical effects. Figure 8 shows the L_2-edge energy dependence of the calculated scattered signal at the $(-\frac{1}{2}0\frac{5}{2})$ node in the π-π' channel within the MST-MT approach. It is compared with the energy dependence of the scattering calculated within the FDM method at the same node and already reported in Fig. 3. The MST-MT energy dependence presents, as the FDM calculated spectrum, a two-peak structure. A quite similar dependence, not shown, is calculated at the other quadrupolar nodes and also at the L_3 edge. However, the slight shift to lower energies of the

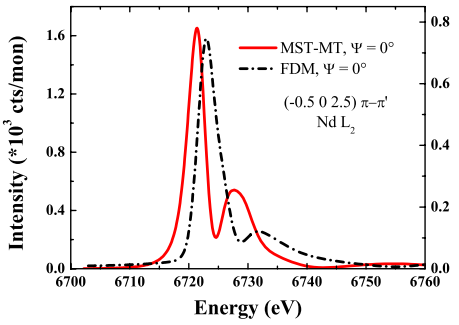

FIG. 8. (Color online) Nd L_2 absorption edge: comparison between the dependence in energy calculated within the MST-MT and the FDM approaches at the $(-\frac{1}{2}0\frac{5}{2})$ quadrupolar node.

MST-MT calculated spectra with respect to the FDM calculated spectra is not understood.

C. Thermal variation of the quadrupolar and magnetic resonant scattering

The thermal evolution of the three reflections, $(-\frac{1}{2}03)$, $(00\frac{5}{2})$, and $(-\frac{1}{2}0\frac{5}{2})$ was followed at the L_2 edge up to 70 K in the π-incident polarization geometry. Figure 9 reports the normalized intensities of the magnetic satellites and the square root of the normalized intensity of the quadrupolar reflection. In the low temperature phase II, the three intensities have an identical thermal variation. Note that the width of the rocking curve scans through the magnetic and quadrupolar satellites, reported in inset of Fig. 9, confirms that the same long-range order is probed. Above T_R only the magnetic reflections remain. The different behavior between the two magnetic reflections at the transition between phases II and I results from the domain reorganization in phase I. Indeed in this phase, the $(-\frac{1}{2}03)$ and $(00\frac{5}{2})$ magnetic satellites arise from two distinct magnetic domains (see Table I). A quadratic dependence on the magnetic order parameter for the scattering at the $(-\frac{1}{2}0\frac{5}{2})$ node brings a full confirmation of the quadrupolar origin of the resonant scattering at this node. A quite similar quadratic dependence on the magnetic moment is also predicted for nonresonant multipolar scattering in magnetically ordered systems.[30]

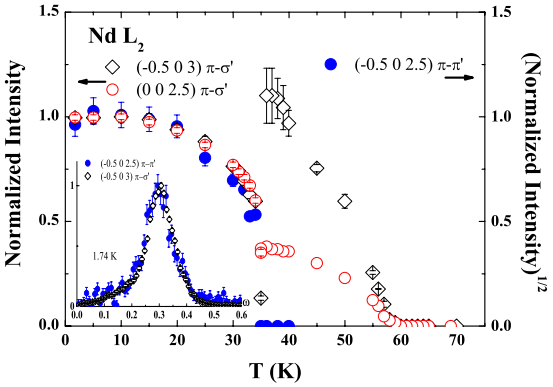

FIG. 9. (Color online) Nd L_2 edge, thermal dependence: (left axis) of the normalized integrated intensities for the $(-\frac{1}{2}03)$ and $(00\frac{5}{2})$ magnetic satellites, (right axis) of the square root of the normalized intensity for the $(-\frac{1}{2}0\frac{5}{2})$ quadrupolar satellite. The inset shows the rocking curve scans through the $(-\frac{1}{2}03)(\pi\text{-}\sigma')$ and $(-\frac{1}{2}0\frac{5}{2})(\pi\text{-}\pi')$ reflections.

V. CONCLUSION

The present experimental and theoretical study of RXS at the $L_{2,3}$ absorption edges of Nd confirms the existence of resonant scattering signals at the reciprocal-space positions associated with both the magnetic and the quadrupolar orderings in phase II of the NdMg compound. Experimentally, the polarization, azimuth, and temperature dependencies of the $(\frac{h}{2}0\frac{l}{2})$-type satellites are fully consistent with the antiferroquadrupolar ordering of the $\langle P_{xy}\rangle$ quadrupolar moment of the Nd ions, ordering that was previously evidenced in nonresonant conditions. The calculations of the resonant quadrupolar scattering performed using the finite-difference method predict the one-peak structure of the energy spectra, the polarization, and azimuth dependencies in noteworthy agreement with the observations. The energy dependence of the magnetic satellites presents a multipeak structure that depends on the edge and on the specular and off-specular character of the reflection. MST-MT calculations including the spin-orbit coupling allow these spectra to be interpreted. The E1 electric dipole transitions toward the $5d$ states give rise to the two peaks at and above the binding energy E_0. Though the monoelectronic approaches are not adapted to describe strongly correlated electrons, the position in energy of the E2 electric quadrupole transitions toward the $4f$ states in the calculated spectra is consistent with the experimental observations at least at the L_3 edge. Quadrupolar scattering is straightforwardly related to the $4f$ orbital asphericity, thus it is expected to be more intense than the magnetic scattering. However, the experiment is observed to be one order of magnitude smaller. This discrepancy likely arises from an unfavorable domain partition in the probed surface crystal. In the same way, the fact that an important nonresonant intensity is detected far below the edges for the off-specular satellites but not for the specular ones can only be ascribed to a strong imbalance in the magnetic domain population. This allows us to emphasize the necessity of having access to the actual domain partition for a quantitative analysis of the magnetic and eventually quadrupolar scattering in antiferromagnets.

ACKNOWLEDGMENTS

The authors are very grateful to T. Moore for his careful reading of the manuscript. This work has been done with the support of the Light Source Theory Network, LighTnet, of the EU.

*oana.bunau@grenoble.cnrs.fr

[1] G. A. Gehring and K. A. Gehring, Rep. Prog. Phys. **38**, 1 (1975).
[2] H. H. Teitelbaum and P. M. Levy, Phys. Rev. B **14**, 3058 (1976).
[3] P. Morin and D. Schmitt, *Ferromagnetic Materials* (Elsevier Science, New York, 1990), Chap. 1, p. 1.
[4] K. N. Lee and B. Bell, Phys. Rev. B **6**, 1032 (1972).
[5] J. Rossat-Mignod, P. Burlet, T. Kasuya, S. Kunii, and T. Komatsubara, Solid State Commun. **39**, 471 (1981).
[6] H. Yamauchi, H. Onodera, K. Ohoyama, T. Onimaru, M. Kosaka, M. Ohashi, and Y. Yamaguchi, J. Phys. Soc. Jpn. **68**, 2057 (1999).
[7] M. Deldem, M. Amara, R. M. Galéra, P. Morin, D. Schmitt, and B. Ouladdiaf, J. Phys.: Condens. Matter **10**, 165 (1998).
[8] M. Amara, R. M. Galéra, P. Morin, and J. F. Berar, J. Phys.: Condens. Matter **10**, L743 (1998).
[9] Y. Murakami, H. Kawada, H. Kawata, M. Tanaka, T. Arima, Y. Moritomo, and Y. Tokura, Phys. Rev. Lett. **80**, 1932 (1998).
[10] Y. Murakami *et al.*, Phys. Rev. Lett. **81**, 582 (1998).
[11] L. Paolasini *et al.*, Phys. Rev. Lett. **82**, 4719 (1999).
[12] I. S. Elfimov, V. I. Anisimov, and G. A. Sawatzky, Phys. Rev. Lett. **82**, 4264 (1999).
[13] Y. Tanaka, T. Inami, T. Nakamura, H. Yamauchi, H. Onodera, K. Ohoyama, and Y. Yamaguchi, J. Phys.: Condens. Matter **11**, L505 (1999).
[14] K. Hirota, N. Oumi, T. Matsumura, H. Nakao, Y. Wakabayashi, Y. Murakami, and Y. Endoh, Phys. Rev. Lett. **84**, 2706 (2000).
[15] S. W. Lovesey and K. S. Knight, Phys. Rev. B **64**, 094401 (2001).
[16] D. F. McMorrow, K. A. McEwen, U. Steigenberger, H. M. Rønnow, and F. Yakhou, Phys. Rev. Lett. **87**, 057201 (2001).
[17] J. A. Paixão, C. Detlefs, M. J. Longfield, R. Caciuffo, P. Santini, N. Bernhoeft, J. Rebizant, and G. H. Lander, Phys. Rev. Lett. **89**, 187202 (2002).
[18] M. J. Longfield, J. A. Paixão, N. Bernhoeft, and G. H. Lander, Phys. Rev. B **66**, 054417 (2002), and references therein.
[19] S. W. Lovesey, E. Balcar, C. Detlefs, G. van der Laan, D. S. Sivia, and U. Staub, J. Phys.: Condens. Matter **15**, 4511 (2003).
[20] N. Bernhoeft, J. A. Paixao, C. Detlefs, S. B. Wilkins, P. Javorsky, E. Blackburn, and G. H. Lander, Phys. Rev. B **69**, 174415 (2004).
[21] S. B. Wilkins, R. Caciuffo, C. Detlefs, J. Rebizant, E. Colineau, F. Wastin, and G. H. Lander, Phys. Rev. B **73**, 060406(R) (2006).
[22] F. Yakhou, V. Plakhty, H. Suzuki, S. Gavrilov, P. Burlet, L. Paolasini, C. Vettier, and S. Kunii, Phys. Lett. A **285**, 191 (2001).
[23] D. Mannix, Y. Tanaka, D. Carbone, N. Bernhoeft, and S. Kunii, Phys. Rev. Lett. **95**, 117206 (2005).
[24] Y. Joly, Phys. Rev. B **63**, 125120 (2001).
[25] Y. Joly, S. Di Matteo, and C. R. Natoli, Phys. Rev. B **69**, 224401 (2004).
[26] O. Bunău and Y. Joly, J. Phys.: Condens. Matter **21**, 345501 (2009).
[27] M. Amara, I. Aviani, S. E. Luca, D. Dufeu, P. Lethuillier, and R. M. Galéra, J. Magn. Magn. Mater. **226-230**, 1005 (2001).
[28] M. Amara, S. E. Luca, R. M. Galéra, I. Aviani, and J. F. Berar, J. Solid State Chem. **171**, 69 (2003).
[29] L. Paolasini *et al.*, J. Synchrotron Radiat. **14**, 301 (2007).
[30] M. Amara, S. E. Luca, and R. M. Galéra, J. Phys.: Condens. Matter **13**, 9621 (2001).
[31] J. P. Hannon, G. T. Trammell, M. Blume, and D. Gibbs, Phys. Rev. Lett. **61**, 1245 (1988).
[32] J. P. Hill and D. F. McMorrow, Acta Crystallogr., Sect. A: Found. Crystallogr. **52**, 236 (1996).
[33] C. Detlefs, Physica B **345**, 45 (2004).
[34] J. A. Bearden and A. F. Burr, Rev. Mod. Phys. **39**, 125 (1967).